ACS APPLIED MATERIALS & INTERFACES

Research Article

www.acsami.org

Facile Synthesis of Graphene-Like Copper Oxide Nanofilms with Enhanced Electrochemical and Photocatalytic Properties in Energy and Environmental Applications

Yang Lu,[†,‡,§] Xianming Liu,[∥] Kangwen Qiu,[†,‡] Jinbing Cheng,[†,‡] Weixiao Wang,[†,‡] Hailong Yan,[†,‡] Chengchun Tang,*[,§] Jang-Kyo Kim,[⊥] and Yongsong Luo*[,†,‡]

[†]School of Physics and Electronic Engineering, Xinyang Normal University, Xinyang 464000, People's Republic of China

[‡]Key Laboratory of Advanced Micro/Nano Functional Materials, Xinyang Normal University, Xinyang 464000, People's Republic of China

[§]School of Material Science and Engineering, Hebei University of Technology, Tianjin 300130, People's Republic of China

[∥]College of Chemistry and Chemical Engineering, Luoyang Normal University, Luoyang 471022, People's Republic of China

[⊥]Department of Mechanical and Aerospace Engineering, Hong Kong University of Science and Technology, Clear Water Bay, Kowloon, Hong Kong, People's Republic of China

Supporting Information

ABSTRACT: Novel graphene-like CuO nanofilms are grown on a copper foam substrate by in situ anodization for multifunctional applications as supercapacitor electrodes and photocatalysts for the degradation of dye pollutants. The as-prepared CuO consists of interconnected, highly crystalline, conductive CuO nanosheets with hierarchical open mesopores and a large surface area. The CuO nanofilms supported on a copper foam are employed as freestanding, binder-free electrodes for supercapacitors, which exhibit wonderful electrochemical performance with a large specific capacitance (919 F g^{-1} at 1 A g^{-1}), an excellent cycling stability (7% capacitance loss after 5000 cycles), and a good rate capability (748 F g^{-1} at 30 A g^{-1}). The porous CuO nanofilms also demonstrate excellent photocatalytic activities for degradation of methylene blue, with a degradation rate 99% much higher than 54% of the commercial CuO powders after 60 min. This excellent energy storage and photocatalytic performance of the graphene-like CuO nanofilms can open a new avenue for large-scale applications in energy and environmental fields.

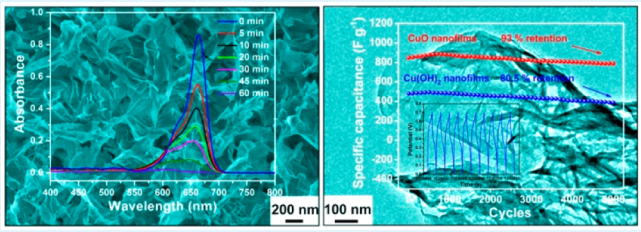

KEYWORDS: *copper oxide, graphene-like nanofilms, anodization, supercapacitor electrode, photocatalyst*

1. INTRODUCTION

In the past decades, copper oxide (CuO) has been extensively applied in photocatalysts (PCs),[1] gas sensors,[2] solar cell devices,[3] and lithium-ion batteries[4] due to its nontoxicity, abundance, and chemical stability.[5,6] With the fast development of nanotechnology, a variety of nanostructural forms of CuO, such as nanotubes,[5] nanowires,[7] nanorods,[8] nanocubes,[9] nanoribbons,[10] hollow structures,[4] and leaf-like structures,[11] have recently been synthesized. The ability to control the shapes and structures of nanomaterials has significant advantages in materials synthesis because the geometry and dimension are key determinants of the physicochemical properties of nanomaterials,[12,13] and thus, the variety of nanostructured CuO would undoubtedly lead to creation of unique characteristics and more extensive applications. For example, pomponlike CuO hollow microspheres[14] were used as anodes for Li-ion batteries, exhibiting a high reversible capacity of 683.7 mAh g^{-1} after 50 cycles at 0.1 C. Chen et al.[15] fabricated porous CuO nanowires for Na-ion batteries, which delivered a discharge capacity of 640 mAh g^{-1} in the first cycle and 303 mA h g^{-1} after 50 cycles at 50 mA g^{-1}. CuO@MnO_2 core−shell nanostructures were applied as electrodes for asymmetric supercapacitors, with an excellent energy density of 22.1 Wh kg^{-1} and a maximum power density of 85.6 kW kg^{-1}.[16]

Graphene, a two-dimensional (2D) sp^2-hybridized carbon sheet with one-atom thickness, has opened new perspectives for carbon nanomaterials due to its exceptional characteristics, including good physical and chemical stability, high specific surface area, high conductivity, and excellent flexibility.[17−19] Inspired by the research and development activities on graphene, graphene-like 2D materials have received renewed attention. For example, ultrathin porous MoS_2 nanosheets were synthesized showing excellent antibacterial activities that were much more potent than that of the precursor MoS_2 powders.[20] Kurungot and co-workers synthesized uniformly porous MnO_2

Received: February 13, 2015
Accepted: April 22, 2015
Published: April 22, 2015

DOI: 10.1021/acsami.5b01451
ACS Appl. Mater. Interfaces 2015, 7, 9682−9690

nanowalls on a conducting carbon fiber substrate that exhibited remarkable electrochemical behavior,[21] while Grätzelet et al. synthesized Fe_2O_3 nanosheets as photoanodes for water photolysis.[22]

The application of 2D nanostructured materials in supercapacitors (SCs) have been particularly popular because their ameliorating attributes, like large surface areas, presence of mesopores (especially with diameters in the range of 2−5 nm), and wide-open geometry, can ensure sufficient active sites and short pathway for charge carriers.[23−25] As for photocatalysts, a large specific surface area is required for the adsorption of reactants, which in turn promotes the reaction between the photogenerated carriers and the reactants, as well as the migration of photogenerated electrons and holes, leading to an enhanced photoactivity.[26,27] Up to now, several fabrication methods have so far been successfully adopted to prepare 2D nanostructures, including hydrothermal process, wet-chemical technique and chemical bath.[28−30] Most of these methods, however, demand strict conditions and complex apparatus, severely limiting the widespread real applications of 2D nanostructures.[31,32]

The present study aims to fabricate porous graphene-like CuO nanofilms using cheap, resourceful and pollution-free materials based on a facile method. The synthesis procedure is illustrated in Figure 1 where the CuO nanofilms are in situ

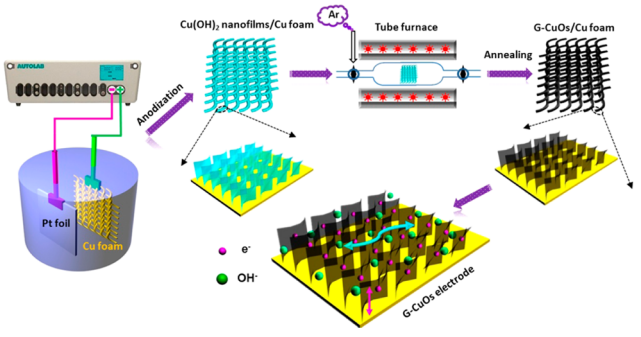

Figure 1. Schematic diagram of direct growth of CuO nanofilms on a Cu foam for SC application.

grown by annealing $Cu(OH)_2$, which is prepared by anodic oxidation of a Cu foam. Anodization, due to its low cost, simplicity, repeatability, and controllability, is a superior approach for large-scale production of 2D nanostructures.[33] This study reports, for the first time, the synthesis of unique graphene-like 2D nanostructures of CuO. The CuO nanofilms with a large surface area over 200 $m^2\ g^{-1}$ and numerous mesopores demonstrate superior performance in multifunctional applications, including supercapacitors and photocatalysts. They deliver specific capacitances (C_s) of 919 and 748 F g^{-1} at current densities of 1 and 30 A g^{-1}, respectively. When used as the photocatalysts, they exhibit photocatalytic activities much better than commercial CuO powders in photodecoloration of methylene blue (MB) dyes in the presence of visible light.

2. EXPERIMENTAL SECTION

2.1. Materials Preparation. Cu foam was selected as the base material for SC electrodes and photocatalysts for the following reasons: (1) it has an excellent electric conductivity, ductility and high corrosion resistance; (2) it can serve as a precursor for CuO nanofilms; (3) the three-dimensional (3D) open space of the foam promotes the flow of electrolyte/sewage, and (4) the foam framework supports ultra-large external surface in comparison with the Cu mesh or foil. All chemicals were of analytical grade and used as received. Before anodization, the Cu foam (99.9% purity, 150 pores per inch, 98% porosity and ∼1.0 mm thick) were cleaned thoroughly in acetone, ethanol, and deionized water and dried in a nitrogen stream. The synthetic experiment was performed in an electrochemical cell using a copper foam working electrode (2.0 × 1.0 cm) and a Pt sheet counter electrode (about 1.6 × 1.0 cm). The electrolyte was 3 M KOH aqueous solution containing 0.07 M cetyltrimethylammonium bromide (CTAB), and the solution was deaerated using a dry nitrogen stream to maintain a slight overpressure throughout the experiment. A constant current density of 1 mA cm^{-2} was applied to the copper foam for 20 min to prepared pale-blue $Cu(OH)_2$ films. Then, the nanofilms were dehydrated at 150 °C for 3 h and finally annealed at 200 °C for 2 h to obtain CuO nanofilms under argon flow.

2.2. Characterization. Both the thermogravimetric and differential thermal analyses (TG-DTA) were performed on a SDT 2960 thermal analyzer at a ramping rate of 10 °C under a stream of N_2. The morphologies and structures of the samples were characterized using the scanning electron microscopy (SEM, JEOL S-4800), transmission electron microscopy (TEM, JEOL 2010), and X-ray diffraction (XRD) spectroscope (Bruker-D8 Germany). Raman spectra were recorded on a laser Raman spectrometer (Renishaw, England) with a 532 nm laser. Fourier transform infrared (FTIR) spectra were obtained in the wave numbers of 400−1200 cm^{-1} at room temperature on a FTIR spectrometer (Thermo Scientific Systems, Nicolet-6700). A Veeco Multimode atomic force microscopy (AFM) was used to obtained surface morphologies. N_2 adsorption/desorption isotherms were obtained on a Micrometritics ASAP 2020 analyzer at 77 K. The pore size distributions of nanofilms were calculated from the desorption branch of the isotherms using the Barrett−Joyner−Halenda (BJH) method.

2.3. Electrochemical Measurements. As a composite electrode, CuO nanofilms/Cu foam was directly used in supercapacitors. The average mass loading of CuO on a Cu foam was 2.5 mg cm^{-2}. The pseudocapacitive performance of the composite electrodes was tested in a three-electrode system using a CHI660E electrochemical workstation. The composite electrode was used as the working electrode, while a Pt foil and a saturated Ag/AgCl served as the counter and reference electrodes, respectively. The electrolyte was a 3 M KOH aqueous solution. Cyclic voltammetry (CV) analyses were conducted between 0 and 0.7 V at different scan rates of 10−200 mV s^{-1}. Galvanostatic charge/discharge (CD) tests were performed with current densities of 1−30 A g^{-1}. Electrochemical impedance spectroscopy (EIS) was carried out in the frequency range of 0.01 Hz to 100 kHz at the open circuit potential with an AC voltage of 5 mV.

2.4. Photocatalytic Measurements. The photocatalytic activities of the CuO nanofilms were examined by the degradation of MB under visible irradiation. In the experiment, 2 mL of 30% H_2O_2 and 2 cm^2 CuO nanofilm photocatalysts were added into 100 mL of 20 mg L^{-1} MB solution in a quartz vessel, and the solution was stirred for 30 min in the dark to achieve the absorption−desorption equilibrium.[34] Then, the mixed solution was exposed to visible light irradiation using a 500 W xenon lamp equipped with a wave filter (λ > 400 nm). At regular intervals, 5 mL of reaction solution was sampled and analyzed by a UV−visible spectrophotometer (UV 2100, Shimadzu).

3. RESULTS AND DISCUSSION

3.1. Structures and Morphologies. The growth of graphene-like $Cu(OH)_2$ nanofilms (Figure S1, Supporting Information) was an electrochemical process where CTAB only served as a template for the formation of the nanofilms. The reactions can be expressed as

$$\text{Anode: } Cu - 2e^- \rightarrow Cu^{2+} \quad (1)$$

$$Cu^{2+} + 2OH^- \rightarrow Cu(OH)_2\downarrow \quad (2)$$

DOI: 10.1021/acsami.5b01451
ACS Appl. Mater. Interfaces 2015, 7, 9682−9690

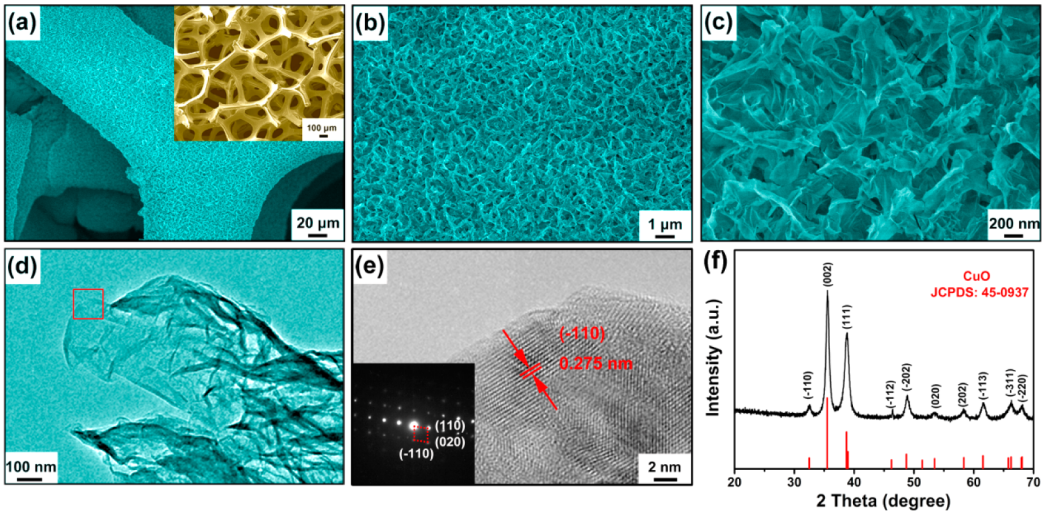

Figure 2. Morphologies and characteristics of CuO nanofilms: (a–c) SEM images taken at different magnifications; (d) low-magnification TEM image; (e) high-resolution TEM image; (f) XRD pattern. (Inset, a) SEM image of bare Cu foam and (inset, e) corresponding SAED pattern from the CuO nanofilms.

$$\text{Cathode: } 2H^+ + 2e^- \rightarrow H_2\uparrow \quad (3)$$

After the heat treatments at 150 °C (for 3 h) and 200 °C (for 2 h) in an Ar atmosphere, the graphene-like morphology of $Cu(OH)_2$ remained largely intact, which was possible due to the robust support of the Cu foam with a relatively large diameter. The morphologies and structures of the final product CuO nanofilms on Cu foam are presented in Figure 2. As shown in Figures 2a,b, a large volume of nanofilms can be obtained with uniform 3D hierarchical architecture compared to that of bare Cu foam (Figure 2a, inset). The nanostructure consisted of interconnected ultrathin CuO films with surrounding nanoscale pores exposed to the surface (Figure 2c). The low magnification TEM image displays that individual CuO nanofilms has a graphene-like flexible and folded structure (Figure 2d). AFM image and the corresponding thickness analysis (Figure S2, Supporting Information) reveal that they are monolayer CuO sheets (with a thickness of ~2 nm) and the size of most of the sheets is larger than 200 nm. The HRTEM image of the selected area marked by a square in Figure 2d reveals that the nanosheet exhibited a fine crystalline nature with an interplanar spacing of 0.275 nm, corresponding to the CuO ($\bar{1}10$) crystal plane (Figure 2e). The single crystalline structure was proved by the regular diffraction spots in the SAED pattern (Figure 2e, inset). The corresponding XRD pattern in Figure 2f shows that all the diffraction peaks are readily indexed to the monoclinic CuO crystals, a reflection of pure CuO nanofilms (JCPDS Card No. 45-0937), in agreement with the above findings.

The high purity nanofilms were further evidenced by the FTIR and Raman spectra, as shown in Figure 3. The FTIR spectrum (Figure 3a) was used to investigate the formation of nanofilms. For CuO, the absorption peaks at 607, 511, and 427 cm^1 are assigned to the Au mode and 2Bu modes, respectively.[35] Among them, the peak at 607 cm^{-1} was related to the stretching vibrations of CuO along the [101] direction, while the peak at 511 cm^1 should be attributed to Cu–O stretching vibration along the [101] direction.[36] Moreover, no extra peaks were present owing to the use of organic surfactants, and no other infrared active modes were observed, like Cu_2O which normally appears at 615 cm^{-1}. These

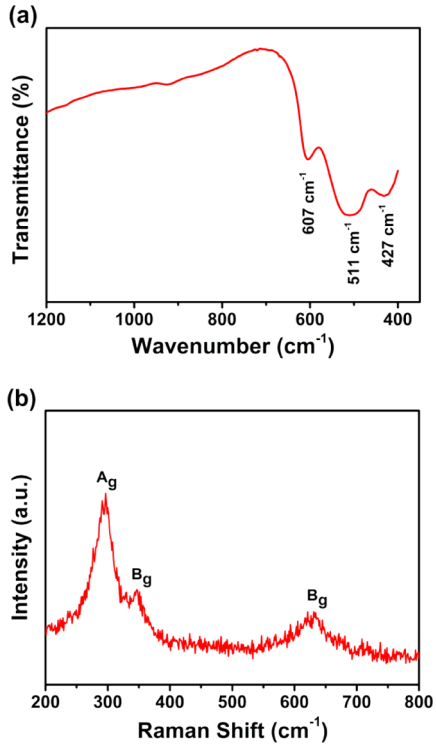

Figure 3. (a) FTIR and (b) Raman spectra of CuO nanofilms.

observations confirmed that the as-obtained final product was pure-phase CuO with a monoclinic structure. The Raman spectrum in the range of 200–800 cm^{-1} (Figure 3b) had a broad peak with a relatively high intensity at 296 cm^{-1} ascribed to A_g band and two peaks at 346 and 630 cm^{-1} ascribed to $2B_g$.[31] The significant intensities of the three peaks also manifest the monoclinic structure with a pure CuO phase, in good agreement with the XRD, FTIR, and SEM results.

The results from TG-DTA of $Cu(OH)_2$ nanofilms are given in Figure S3 (Supporting Information). As the temperature increased to 600 °C, a total weight loss of about 13.5% was observed. The slight weight loss was seen at temperatures below 150 °C, and a larger weight loss appeared between 150

DOI: 10.1021/acsami.5b01451
ACS Appl. Mater. Interfaces 2015, 7, 9682–9690

and 176 °C. The former should be inferred as the evaporation of adsorbed water, while the latter, with a strong endothermic peak at 170 °C, should be associated with the dehydroxylation and decomposition of $Cu(OH)_2$.[37] No weight loss occurred beyond 200 °C, which was chosen as the reasonable annealing temperature.

The specific surface area and porosity of CuO and $Cu(OH)_2$ nanofilms were studied by nitrogen sorption measurements. Figure 4 displays their N_2 adsorption/desorption isotherms and

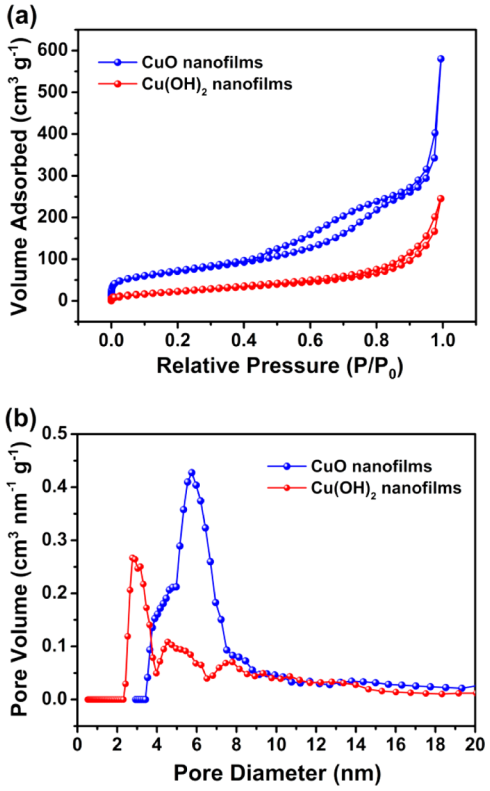

Figure 4. (a) N_2 adsorption/desorption isotherms of CuO and $Cu(OH)_2$ nanofilms and (b) pore size distribution curves obtained from the desorption data.

the corresponding pore-size distribution curves. Both materials exhibited a typical III isotherm with a H3-type hysteresis loop, indicating the presence of mesopores.[5] The BET specific surface area of the CuO nanofilms was 217.4 $m^2\ g^{-1}$, which is 2.4 times larger than that of $Cu(OH)_2$ (90.6 $m^2\ g^{-1}$). The average pore diameters of both nanofilms were placed in the mesopore region: the maxima were centered at 5.85 and 2.76 nm for CuO and $Cu(OH)_2$, respectively. It is well-known that mesopores offer a large electroactive surface area and thus play an ameliorating role in electrochemical reaction due to their capability to promote electrolyte penetration and ion transport. Therefore, the different pore textures of the two materials are likely to affect their performance in energy storage applications.

3.2. Excellent Energy Storage Performance. The freestanding, porous CuO nanofilms on a Cu foam was used as the pseudocapacitive electrode to highlight the merits of the unique architecture for advanced electrochemical capacitor applications. The CV curves of the pristine Cu foam, as-prepared $Cu(OH)_2$, and CuO electrodes obtained at a scan rate of 5 mV s^{-1} are compared in Figure 5a. The C_s of the Cu foam was neglectable while the capacitance of the CuO electrode was higher than the $Cu(OH)_2$ counterpart. The increment of the CV integrated area suggests that the higher capacitance of CuO arose mainly from the much larger surface area and possibly the more mesopores than $Cu(OH)_2$. The CV curves of the CuO electrode taken at different scan rates (Figure 5b) typically presented a pair of well-defined redox peaks, indicating pseudocapacitance as a result of the transition between the oxidation states of Cu^+ and Cu^{2+} species. A redox reaction for the CuO electrode is proposed:[30]

$$2CuO + H_2O + 2e^- \leftrightarrow Cu_2O + 2OH^- \quad (4)$$

As the scan rate increased, the current response subsequently enhanced, meanwhile the shape of the CV curves maintained nearly unaffected. Obviously, in the CV curves, all the response currents on the positive and negative sweeps were almost mirror-image symmetric against each other with respect to the zero-current line, presenting prominent electrochemical reversibility. Indeed, the reversible redox reactions are further confirmed, along with apparent high-rate performance, as shown in Figure 5c. Both the electrochemical cathodic and anodic peak currents varied linearly with scan rate. This implies that the C_s of the CuO electrode originated mainly from pseudocapacitance involved with surface redox reactions and maintained basically stable irrespective of scan rate.[31] C_s was calculated from the cathodic or anodic part of the CV data using the equation[31]

$$C_s = \frac{\int I dV}{\nu \Delta V m} \quad (5)$$

where I (A) is the response current, ν (V s^{-1}) is the potential scan rate, ΔV (V) is the potential window, and m (g) is the mass of the active electrode material. As shown in Figure 5d, the C_s of the CuO electrode gradually lowered from 953 to 862 F g^{-1} as the sweep rate ascended from 10 to 200 mV s^{-1}. The $Cu(OH)_2$ had a similar case with C_s about 589−437 F g^{-1} lower than the corresponding values of the CuO counterpart (Figure 5d and Figure S4a, Supporting Information). The loss of C_s at high charge/discharge rates could be explained by the fact that not all active materials can be participated in the redox reactions.

We probed EIS spectra of the nanofilm electrodes to study the difference in electrochemical performance, as shown in Figure 6a. Both EIS spectra consisted of a semicircle at the high-frequency and a sloped line at the low-frequency. The inset of Figure 6a gives an equivalent circuit used to fit the EIS curves to measure the internal resistance (R_s) and interfacial charge transfer resistance (R_{ct}; Table S1, Supporting Information), where CPE and Z_w are the constant phase element and the Warburg impendence, respectively.[38−40] These results demonstrate that overall pseudocapacitive performance of the CuO electrode were superior to the $Cu(OH)_2$ rival as measured above with reference to Figure 5.

The galvanostatic charge/discharge potentials of the as-prepared CuO and $Cu(OH)_2$ electrode measured between 0 and 0.7 V are shown in Figure 6b and Figure S4b (Supporting Information), respectively. A symmetric triangular shape with well-defined plateaus was observed during the charge/discharge cycles, indicating satisfactory pseudocapacitive behaviors of the two electrodes. The C_s were calculated at different applied current densities using the following equation:

$$C_s = I\Delta t / \Delta V m \quad (6)$$

DOI: 10.1021/acsami.5b01451
ACS Appl. Mater. Interfaces 2015, 7, 9682−9690

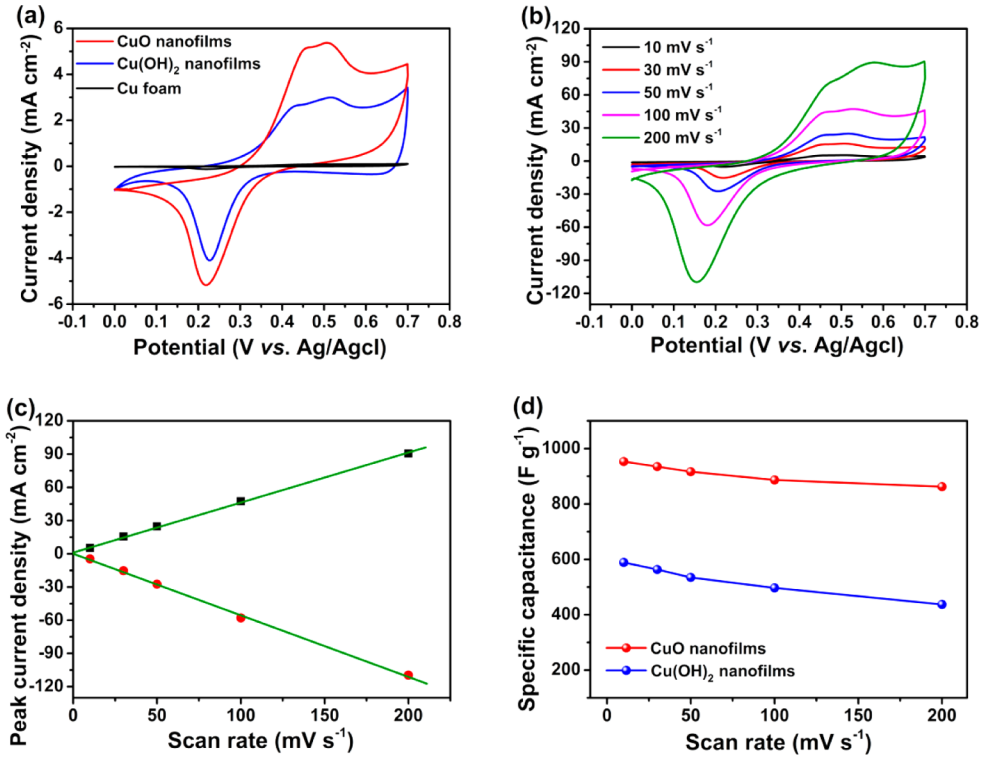

Figure 5. (a) CV curves of different electrode at 10 mV s^{-1}; (b) CV curves of the CuO electrode at various scan rates; (c) plots of peak current versus scan rate for the CuO electrode; and (d) variation of specific capacitance versus scan rate for the CuO and $Cu(OH)_2$ electrodes.

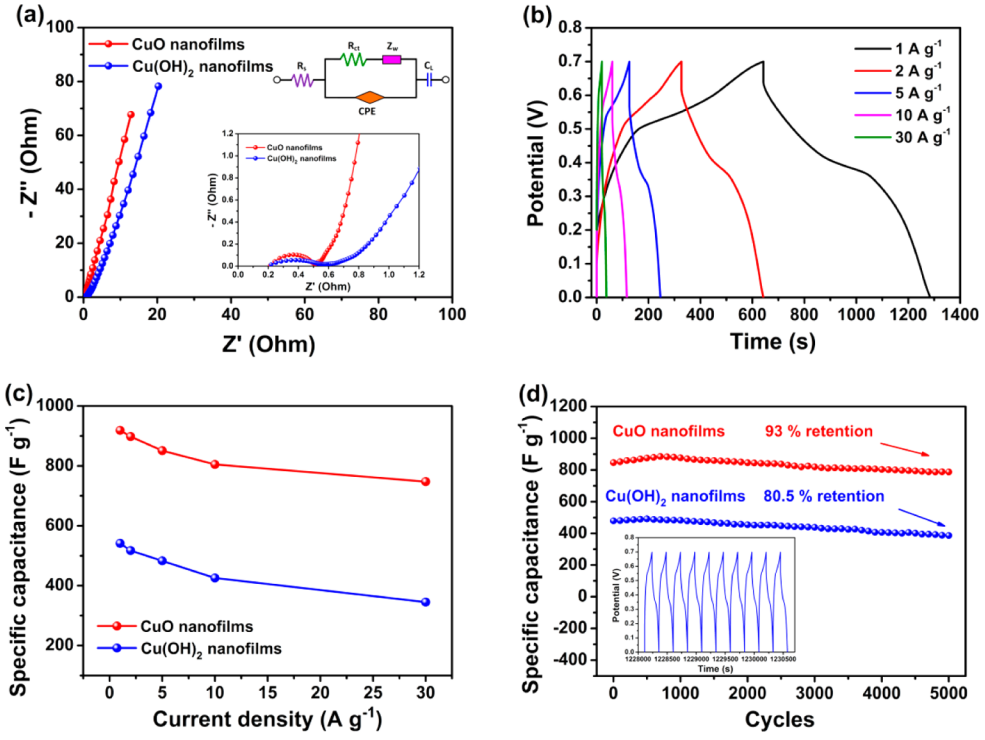

Figure 6. (a) Electrochemical impedance spectra (EIS) of the CuO and $Cu(OH)_2$ electrodes and (inset, top) corresponding equivalent circuit and (inset, bottom) magnified plot; (b) CD curves of the CuO electrode at different current densities; (c) variation of specific capacitance versus current density of the CuO and $Cu(OH)_2$ electrodes; and (d) cyclic performance of the CuO and $Cu(OH)_2$ electrodes at a current density of 5 A g^{-1} and (inset) corresponding CD curves of the last 10 cycles for CuO.

where I and Δt represent the constant discharge current and the total discharge time, respectively. With increasing the current density from 1 to 30 A g^{-1}, the CuO electrode presented a C_s loss of only 19%, which is much smaller than the over 36% loss of the $Cu(OH)_2$ electrode, indicating a superior rate capability of the former electrode (Figure 6c and Figure

DOI: 10.1021/acsami.5b01451
ACS Appl. Mater. Interfaces 2015, 7, 9682−9690

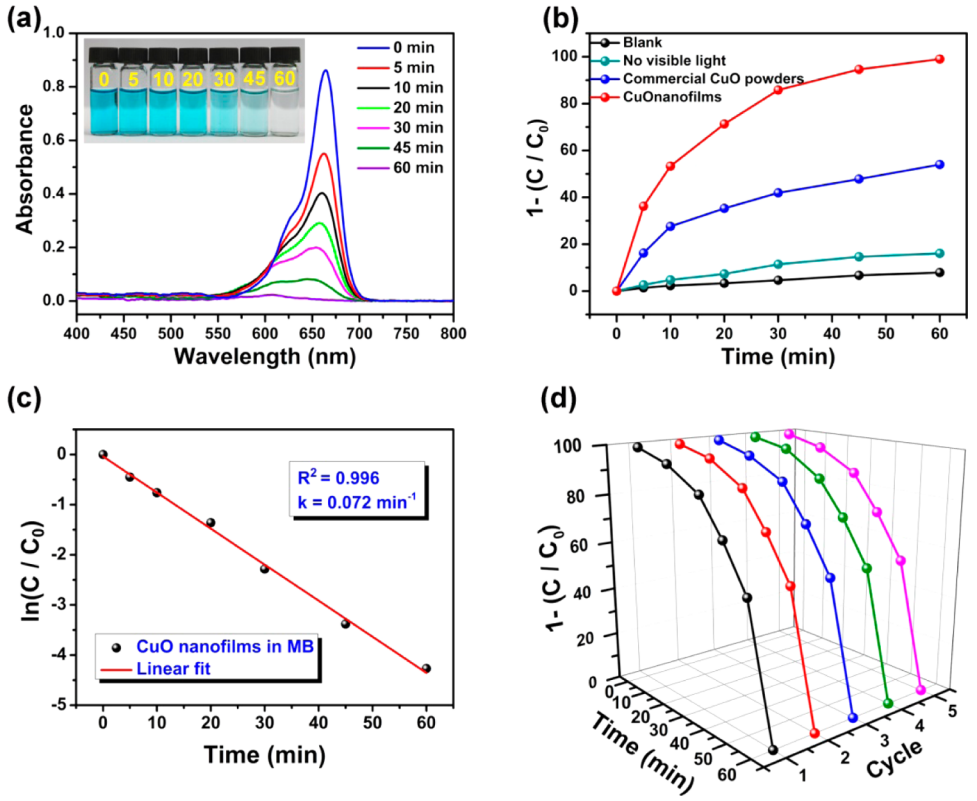

Figure 7. (a) UV−vis absorption spectra and (inset) photographs of the MB solution in the presence of CuO nanofilms after exposure to visible light; (b) adsorption rate of MB concentration with time in water using the initial MB concentration of 20 mg L^{-1}; (c) first-order kinetic plot of $\ln(C_0/C)$ vs time of MB degradation in the presence of CuO nanofilms; and (d) cyclic runs of the photocatalytic degradation of MB in the presence of CuO nanofilms under visible-light.

S4b, Supporting Information). A higher current density meant a greater difference in C_s between the electrodes, confirming that the CuO nanofilms with larger surface areas were more efficient than $Cu(OH)_2$ in maintaining adequate electron transport when charged/discharged at higher rates. The long-term cyclic stability of the electrodes was evaluated at a current density of 5 A g^{-1} for 5000 cycles, as shown in Figure 6d. After the first several hundred cycles, both electrodes achieved the full activation that induced the increase of their C_s. The capacitance retention of the CuO electrode after 5000 cycles was a remarkable 93%, which is well above the 80.5% of the $Cu(OH)_2$ electrode. Moreover, the steady CD curve of the last 10 cycles at 5 A g^{-1} for CuO electrode is also given in the inset of Figure 6d, where the perfect symmetry of charge curves and discharge curves revealed no serious structural collapse of the CuO nanofilms electrode during the charge−discharge processes.[41] Several unique structural features and properties of the CuO/Cu composite structure played a synergistic role to impart the exceptional rate performance and cyclic stability of the electrode, namely, (1) pure and highly crystalline CuO with an excellent electrical conductivity; (2) thin CuO nanofilms firmly deposited on the highly conductive Cu foam substrate, and (3) an interconnected, hierarchical CuO structure with open mesopores and a large surface area.

3.3. Superior Photocatalytic Activity. The photocatalytic activity of a semiconductor is dependent on its energy band structure, which is related to the optical absorption performance.[42] Figure S5 (Supporting Information) shows the UV−vis diffuse reflectance spectra of CuO nanofilms and commercial CuO powders. The CuO nanofilms show a stronger and broader absorption in the visible region compared to the commercial CuO powders, ensuring a higher utilization rate of the solar energy for the enhanced photocatalytic degradations.[43] The band gap (E_g) of the samples can be predicted according to the formula $\alpha h\nu = A(h\nu - E_g)^{n/2}$,[44] where α is the absorption coefficient, h is Planck's constant, ν is the incident light frequency, A is a constant, E_g is the band gap energy, and n depends on the nature of transition (n = 1 for direct transition).[45] The plots of $(\alpha h\nu)^2$ versus photonenergy ($h\nu$) are shown Figure S5 (Supporting Information, inset), from which the band gap energy of CuO samples could be estimated. The estimated E_g of CuO nanofilms and commercial CuO powders from the intercept of the tangents to the plots were 2.28 and 2.44 eV, respectively. Such a difference may be due to the diversities of crystallite phase, morphologies of crystals, defects, and so on.[46]

As typical organic pollutants, MB and rhodamine B are photodegraded in the presence of UV or visible light with the photocatalysis of metal oxide, for instance, $BiVO_4$ and TiO_2.[42,47−50] The photocatalytic activities of the CuO nanofilms for degradation of MB was investigated in the presence of H_2O_2 after exposure to light irradiation. For comparison, the photocatalytic activities of commercial CuO powders were also evaluated, and the results are shown in Figure 7. The UV−vis absorption spectra of the MB aqueous solution in the presence of highly porous CuO showed gradual decreases in MB absorbance peak accompanied by down-shift of the absorbance band when the exposure time increased (Figure 7a). After 60 min, the absorbance band became very broad and weak, demonstrating almost full degradation of MB, as further proven

DOI: 10.1021/acsami.5b01451
ACS Appl. Mater. Interfaces 2015, 7, 9682−9690

by the solution color change (inset photographs of Figure 7a). The MB absorbance peaks, C, obtained at 664 nm were monitored for both the commercial CuO powders and the CuO nanofilms developed in this study. These absorbance values were normalized by those measured after the equilibrium between the photocatalyst and MB before irradiation, which were then subtracted from 1 to obtain the degradation rate ($1 - (C/C_0)$), as a measure of efficiency of photodegradation. This means that the higher the degradation rate, the higher the intensity of photocatalytic activity. The degradation rates are plotted as a function of reaction time for different catalysts under visible light illumination ($\lambda > 400$ nm; Figure 7b). The "blank" test demonstrates that the photolysis of MB was extremely low, with a degradation rate about 8% after 60 min, when there was no photocatalyst (only H_2O_2 was added to the MB solution). The adsorption of MB by the CuO photocatalyst in the dark ("no visible light" in Figure 7b) was also inspected. After 60 min, the concentration of MB decreased by about 16%, proving that the decolorization of MB by CuO was attributed not to adsorption, but essentially to photodegradation. When both CuO and visible irradiation were applied into the MB $+H_2O_2$ system, the degradation effect was significantly promoted. The photocatalytic activity of the CuO nanofilms with a remarkable degradation rate of 99% was much better than the corresponding degradation rate of 54% shown by the commercial CuO powders after 60 min. A larger surface area of the photocatalysts resulted in a higher photocatalytic activity.[42] Because both the CuO nanofilms and the commercial CuO are essentially the same material, the excellent photocatalytic activity is associated with the ultralarge surface area of the CuO nanofilms with open mesopores, making more surfaces readily available for the photogenerated electrons and holes to contact with MB.

Recently, H_2O_2 has been employed as a green additive to stimulate/enhance the photocatalytic activity of metal oxides, because the photolysis of H_2O_2 generates free radical species like HO·, HOO·, or $O_2^{\cdot -}$, which are contributive factors to the efficient degradation of organic dyes.[51,52] In a synthesis of previous studies, the general procedure in the photodegradation of MB can be concluded as (1) first, the MB molecules and H_2O_2 are adsorbed on the surface of the nanofilms; (2) then, H_2O_2 decomposes and releases free radical species, including the mineralization of the dye pollutants; and (3) finally, the photocatalysts regain rapidly after the dye molecules move away from the nanofilm surface.[52,53] All in all, the CuO photocatalysts play a key role in decomposing H_2O_2, and the released free radicals equally have a better positive effect on the prominent photodegradation of MB by the CuO nanofilms in comparison with that of the commercial CuO powders.

Furthermore, the kinetics of degradation was investigated for the MB dye. The photodegradation process of both the CuO nanofilms and commercial CuO powders displayed the pseudo-first-order kinetics model,[52] which can be described by a linear relationship in a natural log plot:[54]

$$\ln(C/C_0) = -kt \quad (7)$$

where k is the reaction constant of the first-order reaction, and t is the reaction time. Figure 7c and Figure S6 (Supporting Information) present the linear plots, $\ln(C/C_0)$ vs t, for the CuO nanofilms and commercial CuO powders, respectively. Both photocatalysts had excellent linear correlations, $R^2 = 0.996$ and 0.909, respectively, suggesting that their degradation reactions indeed followed the first-order kinetics. The slopes of the linear lines gave the first-order rate constants, which were 0.072 and 0.012 min^{-1}, respectively, further confirming a much higher photocatalytic efficiency of the CuO nanofilms than the commercial CuO powders.

To evaluate the stability of the photocatalytic activity of the CuO nanofilms, we repeated the cycle tests in the photodegradation of MB treated with visible light for five cycles, and the results are shown in Figure 7d. It is worth noting that there was a negligible decline in photocatalytic activity with less than 2% reduction after five cyclic runs. This observation verifies exceptionally high stability of the CuO nanofilm photocatalysts, which seldom photocorrode during the photocatalytic oxidation of the model pollutant molecules. The excellent photocatalytic activities and stability of the CuO nanofilms mean their potential large-scale application as a visible-light driven catalyst.

4. CONCLUSIONS

Novel graphene-like CuO nanofilms were successfully prepared using the anodization method followed by thermal treatments. Various characterization tools were employed to identify prominent structural, morphological and elemental features of the CuO nanofilms. CuO nanofilms consisted of interconnected, highly crystalline nanosheets, and possessed open mesopores, a large specific surface area and a high electrical conductivity. They delivered remarkable electrochemical performance and cyclic stability when used as the electrodes for supercapacitors. In addition, they also presented excellent photocatalytic activities for the degradation of MB when the MB aqueous solution was exposed to visible light. The unique architectural features of the CuO nanofilms with a large surface area and open mesopores played a synergistic role to impart such interesting multifunctional characteristics. These observations suggest that the novel materials can find many potential applications, not only in supercapacitors and sewage treatments, but also in broad fields, such as energy storage in other rechargeable batteries, water splitting, and nonenzymatic glucose biosensors.

■ ASSOCIATED CONTENT

Supporting Information

TG-DTA curves, SEM image, XRD pattern and electrochemical characterization of $Cu(OH)_2$ nanofilms, and first-order kinetic plot of commercial CuO powders. The Supporting Information is available free of charge on the ACS Publications website at DOI: 10.1021/acsami.5b01451.

■ AUTHOR INFORMATION

Corresponding Authors

*E-mail: tangcc@hebut.edu.cn.
*E-mail: ysluo@xynu.edu.cn.

Notes

The authors declare no competing financial interest.

■ ACKNOWLEDGMENTS

This work was financially supported by the National Natural Science Foundation of China (Nos. U1304108, U1204501, and 21373107) and the Innovative Research Team (in Science and Technology) of the University of Henan Province (No. 13IRTSTHN018).

DOI: 10.1021/acsami.5b01451
ACS Appl. Mater. Interfaces 2015, 7, 9682−9690

REFERENCES

(1) Switzer, J. A.; Kothari, H. M.; Poizot, P.; Nakanishi, S.; Bohannan, E. W. Enantiospecific Electrodeposition of a Chiral Catalyst. *Nature* **2003**, *425*, 490−493.

(2) Zhu, G. X.; Xu, H.; Xiao, Y. Y.; Liu, Y. J.; Yuan, A. H.; Shen, X. P. Facile Fabrication and Enhanced Sensing Properties of Hierarchically Porous CuO Architectures. *ACS Appl. Mater. Interfaces* **2012**, *4*, 744−751.

(3) Liu, Y. L.; Liao, L.; Li, J. C.; Pan, C. X. From Copper Nanocrystalline to CuO Nanoneedle Arrays: Synthesis, Growth Mechanism, and Properties. *J. Phys. Chem. C* **2007**, *111*, 5050−5056.

(4) Park, J. C.; Kim, J.; Kwon, H.; Song, H. Gram-Scale Synthesis of Cu_2O Nanocubes and Subsequent Oxidation to CuO Hollow Nanostructures for Lithium-Ion Battery Anode Materials. *Adv. Mater.* **2009**, *21*, 803−807.

(5) Lu, Y.; Qiu, K. W.; Zhang, D. Y.; Lin, J.; Xu, J. Y.; Liu, X. M.; Tang, C. C.; Kim, J. K.; Luo, Y. S. Cost-Effective CuO Nanotube Electrodes for Energy Storage and Non-Enzymatic Glucose Detection. *RSC Adv.* **2014**, *4*, 46814−46822.

(6) Banerjee, A.; Singh, U.; Aravindan, V.; Srinivasan, M.; Ogale, S. Synthesis of CuO Nanostructures from Cu-Based Metal Organic Framework (MOF-199) for Application as Anode for Li-Ion Batteries. *Nano Energy* **2013**, *2*, 1158−1163.

(7) Tao, A.; Kim, F.; Hess, C.; Goldberger, J.; He, R. R.; Sun, Y. G.; Xia, Y. N.; Yang, P. D. Langmuir−Blodgett Silver Nanowire Monolayers for Molecular Sensing Using Surface-Enhanced Raman Spectroscopy. *Nano Lett.* **2003**, *3*, 1229−1233.

(8) Dumestre, F.; Chaudret, B.; Amiens, C.; Fromen, M. C.; Casanove, M. J.; Renaud, P.; Zurcher, P. Shape Control of Thermodynamically Stable Cobalt Nanorods Through Organometallic Chemistry. *Angew. Chem., Int. Ed.* **2002**, *41*, 4286−4289.

(9) Sun, Y. G.; Xia, Y. N. Shape-Controlled Synthesis of Gold and Silver Nanoparticles. *Science* **2002**, *298*, 2176−2179.

(10) Liu, B.; Zeng, H. C. Mesoscale Organization of CuO Nanoribbons: Formation of "Dandelions". *J. Am. Chem. Soc.* **2004**, *126*, 8124−8125.

(11) Zhao, B.; Liu, P.; Zhuang, H.; Jiao, Z.; Fang, T.; Xu, W. W.; Lu, B.; Jiang, Y. Hierarchical Self-Assembly of Microscale Leaf-Like CuO on Graphene Sheets for High-Performance Electrochemical Capacitors. *J. Mater. Chem. A* **2013**, *1*, 367−373.

(12) Wang, C.; Higgins, D.; Wang, F. F.; Li, D. Y.; Liu, R. Q.; Xia, G. F.; Li, N.; Xu, H.; Wu, G. Controlled Synthesis of Micro/Nanostructured CuO Anodes for Lithium-Ion Batteries. *Nano Energy* **2014**, *9*, 334−344.

(13) Yang, X. L.; Wang, X. Y.; Liu, X. Z.; Zhang, Y. J.; Song, W. G.; Shu, C. Y.; Jiang, L.; Wang, C. R. Preparation of Graphene-Like Iron Oxide Nanofilm/Silica Composite with Enhanced Adsorption and Efficient Photocatalytic Properties. *J. Mater. Chem. A* **2013**, *1*, 8332−8337.

(14) Wang, J.; Liu, Y. C.; Wang, S. Y.; Guo, X. T.; Liu, Y. P. Facile Fabrication of Pompon-Like Hierarchical CuO Hollow Microspheres for High-Performance Lithium-Ion Batteries. *J. Mater. Chem. A* **2014**, *2*, 1224−1229.

(15) Wang, L. J.; Zhang, K.; Hu, Z.; Duan, W. C.; Cheng, F. Y.; Chen, J. Porous CuO Nanowires as the Anode of Rechargeable Na-Ion Batteries. *Nano Res.* **2014**, *7*, 199−208.

(16) Huang, M.; Zhang, Y. X.; Li, F.; Wang, Z. C.; Alamusi, H. N.; Wen, Z. Y.; Liu, Q. Merging of Kirkendall Growth and Ostwald Ripening: CuO@MnO_2 Core-Shell Architectures for Asymmetric Supercapacitors. *Sci. Rep.* **2014**, *4*, 4518.

(17) Huang, X.; Yin, Z. Y.; Wu, S. X.; Qi, X. Y.; He, Q. Y.; Zhang, Q. C.; Yan, Q. Y.; Boey, F.; Zhang, H. Graphene-Based Materials: Synthesis, Characterization, Properties, and Applications. *Small* **2011**, *7*, 1876−1902.

(18) Lee, C. G.; Wei, X. D.; Kysar, J. W.; Hone, J. Measurement of the Elastic Properties and Intrinsic Strength of Monolayer Graphene. *Science* **2008**, *321*, 385−388.

(19) Hu, C. G.; Song, L.; Zhang, Z. P.; Chen, N.; Feng, Z. H.; Qu, L. T. Tailored Graphene Systems for Unconventional Applications in Energy Conversion and Storage Devices. *Energy Environ. Sci.* **2015**, *8*, 31−34.

(20) Yang, X.; Li, J.; Liang, T.; Ma, C. Y.; Zhang, Y. Y.; Chen, H. Z.; Hanagata, N.; Su, H. X.; Xu, M. S. Antibacterial Activity of Two-Dimensional MoS_2 Sheets. *Nanoscale* **2014**, *6*, 10126−10133.

(21) Anothumakkool, B.; Kurungot, S. Electrochemically Grown Nanoporous MnO_2 Nanowalls on a Porous Carbon Substrate with Enhanced Capacitance through Faster Ionic and Electrical Mobility. *Chem. Commun.* **2014**, *50*, 7188−7190.

(22) Cesar, I.; Kay, A.; Martinez, J. A. G.; Grätzel, M. Translucent Thin Film Fe_2O_3 Photoanodes for Efficient Water Splitting by Sunlight: Nanostructure-Directing Effect of Si-Doping. *J. Am. Chem. Soc.* **2006**, *128*, 4582−4583.

(23) Lu, Y.; Yan, H. L.; Zhang, D. Y.; Qiu, K. W.; Lin, J.; Xue, Y. M.; Li, J.; Tang, C. C.; Luo, Y. S. Hybrid Nanonet/Nanoflake $NiCo_2O_4$ Electrodes with an Ultrahigh Surface Area for Supercapacitors. *J. Solid State Electrochem.* **2014**, *18*, 3143−3152.

(24) Futaba, D. N.; Hata, K.; Yamada, T.; Hiraoka, T.; Hayamizu, Y.; Kakudate, Y.; Tanaike, O.; Hatori, H.; Yumura, M.; Iijima, S. Shape-Engineerable and Highly Densely Packed Single-Walled Carbon Nanotubes and Their Application as Super-Capacitor Electrodes. *Nat. Mater.* **2006**, *5*, 987−994.

(25) Zhou, H. S.; Li, D. L.; Hibino, M.; Honma, I. A Self-Ordered, Crystalline-Glass, Mesoporous Nanocomposite for Use as a Lithium-Based Storage Device with Both High Power and High Energy Densities. *Angew. Chem., Int. Ed.* **2005**, *44*, 797−802.

(26) Ke, D. N.; Peng, T. Y.; Ma, L.; Can, P.; Dai, K. Effects of Hydrothermal Temperature on the Microstructures of $BiVO_4$ and Its Photocatalytic O_2 Evolution Activity under Visible Light. *Inorg. Chem.* **2009**, *48*, 4685−4691.

(27) Bao, N. Z.; Shen, L. M.; Takata, T.; Domen, K. Self-Templated Synthesis of Nanoporous CdS Nanostructures for Highly Efficient Photocatalytic Hydrogen Production under Visible Light. *Chem. Mater.* **2008**, *20*, 110−117.

(28) Liu, J.; Jin, J.; Deng, Z.; Huang, S. Z.; Hu, Z. Y.; Wang, L.; Wang, C.; Chen, L. H.; Li, Y.; Tendeloo, G. V.; Su, B. L. Tailoring CuO Nanostructures for Enhanced Photocatalytic Property. *J. Colloid Interface Sci.* **2012**, *384*, 1−9.

(29) Lu, C. H.; Qi, L. M.; Yang, J. H.; Zhang, D. Y.; Wu, N. Z.; Ma, J. M. Simple Template-Free Solution Route for the Controlled Synthesis of $Cu(OH)_2$ and CuO Nanostructures. *J. Phys. Chem. B* **2004**, *108*, 17825−17831.

(30) Wang, G. L.; Huang, J. C.; Chen, S. L.; Gao, Y. Y.; Cao, D. X. Preparation and Supercapacitance of CuO Nanosheet Arrays Grown on Nickel Foam. *J. Power Sources* **2011**, *196*, 5756−5760.

(31) Lu, Y.; Yan, H. L.; Qiu, K. W.; Cheng, J. B.; Wang, W. X.; Liu, X. M.; Tang, C. C.; Kim, J. K.; Luo, Y. S. Hierarchical Porous CuO Nanostructures with Tunable Properties for High Performance Supercapacitors. *RSC Adv.* **2015**, *5*, 10773−10781.

(32) Xie, K. Y.; Li, J.; Lai, Y. Q.; Lu, W.; Zhang, Z. A.; Liu, Y. X.; Zhou, L. M.; Huang, H. T. Highly Ordered Iron Oxide Nanotube Arrays as Electrodes for Electrochemical Energy Storage. *Electrochem. Commun.* **2011**, *13*, 657−660.

(33) Zhang, W. Y.; Xi, Z. P.; Li, G. Z.; Wang, Q. B.; Tang, H. P.; Liu, Y.; Zhao, Y.; Jiang, L. Highly Ordered Coaxial Bimodal Nanotube Arrays Prepared by Self-Organizing Anodization on Ti Alloy. *Small* **2009**, *5*, 1742−1746.

(34) Lv, X. J.; Zhang, H.; Chang, H. X. Improved Photocatalytic Activity of Highly Ordered TiO_2 Nanowire Arrays for Methylene Blue Degradation. *Mater. Chem. Phys.* **2012**, *136*, 789−795.

(35) Zou, G. F.; Li, H.; Zhang, D. W.; Xiong, K.; Dong, C.; Qian, Y. T. Well-Aligned Arrays of CuO Nanoplatelets. *J. Phys. Chem. B* **2006**, *110*, 1632−1637.

(36) Kliche, K.; Popovic, Z. V. Far-Infrared Spectroscopic Investigations on CuO. *Phys. Rev. B: Condens. Matter* **1990**, *42*, 10060−10066.

(37) Zhang, Y. X.; Huang, M.; Li, F.; Wen, Z. Q. Controlled Synthesis of Hierarchical CuO Nanostructures for Electrochemical Capacitor Electrodes. *Int. J. Electrochem. Sci.* **2013**, *8*, 8645−8661.

DOI: 10.1021/acsami.5b01451
ACS Appl. Mater. Interfaces 2015, 7, 9682−9690

(38) Luo, Y. S.; Luo, J. S.; Jiang, J.; Zhou, W. W.; Yang, H. P.; Qi, X. Y.; Zhang, H.; Fan, H. J.; Yu, D. Y. W.; Li, C. M.; Yu, T. Seed-Assisted Synthesis of Highly Ordered TiO_2@a-Fe_2O_3 Core/Shell Arrays on Carbon Textiles for Lithium-Ion Battery Applications. *Energy Environ. Sci.* **2012**, *5*, 6559−6566.
(39) Laheäär, A.; Jänes, A.; Lust, E. $NaClO_4$ and $NaPF_6$ as Potential Non-Aqueous Electrolyte Salts for Electrical Double Layer Capacitor Application. *Electrochim. Acta* **2012**, *82*, 309−313.
(40) Zhang, B.; Liu, Y.; Huang, Z. D.; Oh, S. W.; Yu, Y.; Mai, Y. W.; Kim, J. K. Urchin-like $Li_4Ti_5O_{12}$-Carbon Nanofiber Composites for High Rate Performance Anodes in Li-Ion Batteries. *J. Mater. Chem.* **2012**, *22*, 12133−12140.
(41) Luo, Y. S.; Kong, D. Z.; Luo, J. S.; Chen, C.; Zhang, D. Y.; Qiu, K. W.; Qi, X. Y.; Zhang, H.; Li, C. M.; Yu, T. Hierarchical TiO_2 Nanobelts@MnO_2 Ultrathin Nanoflakes Core-Shell Array Electrode Materials for Supercapacitors. *RSC Adv.* **2013**, *3*, 14413−14422.
(42) Lu, Y.; Luo, Y. S.; Xiao, H. M.; Fu, S. Y. Novel Core-Shell Structured $BiVO_4$ Hollow Spheres with an Ultra-High Surface Area as Visible-Light-Driven Catalyst. *CrystEngComm* **2014**, *16*, 6059−6065.
(43) Li, G. P.; Mao, L. Q. Magnetically Separable Fe_3O_4-Ag_3PO_4 Sub-Micrometer Composite: Facile Synthesis, High Visible Light-Driven Photocatalytic Efficiency, and Good Recyclability. *RSC Adv.* **2012**, *2*, 5108−5111.
(44) Butler, M. A. Photoelectrolysis and Physical Properties of the Semiconducting Electrode WO_3. *J. Appl. Phys.* **1977**, *48*, 1914−1920.
(45) Kaur, M.; Muthe, K. P.; Despande, S. K.; Choudhury, S.; Singh, J. B.; Verma, N.; Gupta, S. K.; Yakhmi, J. V. Growth and Branching of CuO Nanowires by Thermal Oxidation of Copper. *J. Cryst. Growth* **2006**, *289*, 670−675.
(46) Zhang, M. L.; An, T. C.; Hu, X. H.; Wang, C.; Sheng, G. Y.; Fu, J. M. Preparation and Photocatalytic Properties of a Nanometer ZnO-SnO_2 Coupled Oxide. *Appl. Catal. A: Gen* **2004**, *260*, 215−220.
(47) Lu, Y.; Luo, Y. S.; Kong, D. Z.; Zhang, D. Y.; Jia, Y. L.; Zhang, X. W. Large-Scale Controllable Synthesis of Dumbbell-Like $BiVO_4$ Photocatalysts with Enhanced Visible-Light Photocatalytic Activity. *J. Solid State Chem.* **2012**, *186*, 255−260.
(48) Batista, A. P. L.; Carvalho, H. W. P.; Luz, G. H. P.; Martins, P. F. Q.; Goncalves, M.; Oliveira, L. C. A. Preparation of CuO/SiO_2 and Photocatalytic Activity by Degradation of Methylene Blue. *Environ. Chem. Lett.* **2010**, *8*, 63−67.
(49) Xie, Z.; Liu, X. X.; Wang, W. P.; Wang, X. J.; Liu, C.; Xie, Q.; Li, Z. C.; Zhang, Z. J. Enhanced Photoelectrochemical and Photocatalytic Performance of TiO_2 Nanorod Arrays/CdS Quantum Dots by Coating TiO_2 through Atomic Layer Deposition. *Nano Energy* **2015**, *11*, 400−408.
(50) Xu, H.; Zhu, G. X.; Zheng, D.; Xi, C. Y.; Xu, X.; Shen, X. P. Porous CuO Superstructure: Precursormediated Fabrication, Gas Sensing and Photocatalytic Properties. *J. Colloid Interface Sci.* **2012**, *383*, 75−81.
(51) Mageshwari, K.; Sathyamoorthy, R.; Park, J. Photocatalytic Activity of Hierarchical CuO Microspheres Synthesized by Facile Reflux Condensation Method. *Powder Technol.* **2015**, *270*, 150−156.
(52) Zaman, S.; Zainelabdin, A.; Amin, G.; Willander, O. N. M. Efficient Catalytic Effect of CuO Nanostructures on the Degradation of Organic Dyes. *J. Phys. Chem. Solids* **2012**, *73*, 1320−1325.
(53) Zhang, W. X.; Yang, Z. H.; Wang, X.; Zhang, Y. C.; Wen, X. G.; Yang, S. H. Large-Scale Synthesis of β-MnO_2 Nanorods and Their Rapid and Efficient Catalytic Oxidation of Methylene Blue Dye. *Catal. Commun.* **2006**, *7*, 408−412.
(54) Mehrdad, A.; Massoumi, B.; Hashemzadeh, R. Kinetic Study of Degradation of Rhodamine B in the Presence of Hydrogen Peroxide and Some Metal Oxide. *Chem. Eng. J.* **2011**, *168*, 1073−1078.

DOI: 10.1021/acsami.5b01451
ACS Appl. Mater. Interfaces 2015, 7, 9682−9690